2014

Exploiting superior tensile properties of a novel network-structure AlA206 matrix composite by hybridizing micron-sized Al3Ti with Al2O3 nano particulates

S Tahamtan
University of Tehran

A Halvaee
University of Tehran

M Emamy
University of Tehran

Z Y. Jiang
University of Wollongong, jiang@uow.edu.au

A Fadavi Boostani
University of Wollongong, afb496@uowmail.edu.au

Publication Details

Tahamtan, S., Halvaee, A., Emamy, M., Jiang, Z. Y. & Boostani, A. Fadavi. (2014). Exploiting superior tensile properties of a novel network-structure AlA206 matrix composite by hybridizing micron-sized Al3Ti with Al2O3 nano particulates. Journal of Materials Science and Engineering A, 619 190-198.

Exploiting superior tensile properties of a novel network-structure AlA206 matrix composite by hybridizing micron-sized Al3Ti with Al2O3 nano particulates

Abstract
In this study, semi-solid stir casting and ball milling processes are combined into an integrated composite fabrication process. Two different architectures were utilized to incorporate reinforcing particle into semi-solid alloy i.e., (i) ball milling of K2TiF6 and aluminum powder for 5h and subsequently with nano-alumina particles (Al2O3np) for 1h and (ii) ball milling of K2TiF6, Al2O3np and aluminum powder for 2h. Accordingly, the milled powders were incorporated into molten AlA206 alloy using a non-contact ultrasonic vibration method. The effect of milling procedure on microstructural evolution and tensile properties were then explored. Two different microstructures were characterized including well-distributed Al2O3np and Al3Ti particles (Al3Tip) and a network-structure containing Al3Tip+Al2O3np. This unique architecture of network-structure brought about increment in tensile properties compared to well-distributed reinforcement particles, ascribed to the strewing of Al3Tip+Al2O3np around matrix grain boundaries, act as a three-dimension skeletal structure with high local volume fraction of Al3Tip+Al2O3np.

Disciplines
Engineering | Science and Technology Studies

Publication Details
Tahamtan, S., Halvaee, A., Emamy, M., Jiang, Z. Y. & Boostani, A. Fadavi. (2014). Exploiting superior tensile properties of a novel network-structure AlA206 matrix composite by hybridizing micron-sized Al3Ti with Al2O3 nano particulates. Journal of Materials Science and Engineering A, 619 190-198.

Exploiting superior tensile properties of a novel network-structure AlA206 matrix composite by hybridizing micron-sized Al_3Ti with Al_2O_3 nano particulates

S. Tahamtan[*, a], A. Halvaee[a], M. Emamy[a], A. Fadavi boostani[b], Z.Y. Jiang [b]

[a]School of Metallurgy and Materials Engineering, College of Engineering, University of Tehran, Tehran, Iran.

[b]School of Mechanical, Materials and Mechatronic Engineering, University of Wollongong, NSW 2522, Australia

Abstract

In this study, semi-solid stir casting and ball milling processes are combined into an integrated composite fabrication process. Two different architectures were utilized to incorporate reinforcing particle into semi-solid alloy i.e., (i) ball milling of K_2TiF_6 and aluminium powder for 5 h and subsequently with nano-alumina particles (Al_2O_{3np}) for 1 h and (ii) ball milling of K_2TiF_6, Al_2O_{3np} and aluminum powder for 2 h. Accordingly, the milled powders were incorporated into molten AlA206 alloy using a non-contact ultrasonic vibration method. The effect of milling procedure on microstructural evolution and tensile properties were then explored. Two different microstructures were characterized including well-distributed Al_2O_{3np} and Al_3Ti particles (Al_3Ti_p) and a network-structure containing Al_3Ti_p+Al_2O_{3np}. This unique architecture of network-structure brought about increment in tensile properties compared to well-distributed reinforcement particles, ascribed to the strewing of Al_3Ti_p+Al_2O_{3np} around matrix grain boundaries, act as a three-dimension skeletal structure with high local volume fraction of Al_3Ti_p+Al_2O_{3np}.

Keywords: A206 Alloy; Semi solid processing; Metal matrix composites; Transmission Electron Microscopy; Fracture.

1. Introduction

One of the most important metal matrix composites (MMCs) are aluminum matrix composites (AMCs) reinforced alumina particulates, extensively being used in the aerospace and automobile industries [1-7]. AMCs, especially discontinuously reinforced aluminum matrix composites (DRAMCs) have received large attention because of their augmented tensile and tribological properties [1-8].

[*] Corresponding author. Tel. +98 917 710 8449, Fax. +98 21 6687 2115
Email address: Tahamtan@ut.ac.ir (S. Tahamtan)

DRAMCs with uniformly distributed reinforcement exhibit a certain improvement in partial properties with respect to the matrix alloy [9]. Investigations in the past two decades confirmed that DRAMCs exhibited limited strengthening effect of reinforcement and augmented mechanical properties can be achieved by tailoring the microstructure at a higher level [10-12]. In order to increment the performance of DRAMCs, recent studies have been focused towards exploring three-dimensional microstructures such as bi-continuous, inter-penetrating and quasi-continuous composites [13-15]. As reported by Huang et al. in the case of Ti matrix composites, a controlled three-dimensional microstructure has the capability to enhance the properties of material, such as elastic modulus, tensile strength and fracture toughness, compared with well-distributed counterparts, [13, 15-19].

Beside ceramic reinforcements, trialuminide intermetallics such as Al_3Zr and Al_3Ti have been also used widely as reinforcement [20-24]. Trialuminide intermetallics have some important advantages over ceramic particulates such as low densities, higher thermal stability, good machinibility and formability [25,26]. However, the brittle nature of trialuminide intermetallics can preside over the properties of the composite giving rise to negligible increment in mechanical properties [22]. Therefore, microstructural control is needed to implement Al_3Ti intermetallic as a useful reinforcement in MMCs. Furthermore, using two or more types of particulates in a single matrix, hybrid composites, the benefits of one type of particulates could supplement to what is lacking in the other [27].

This study shows how microstructural control can be used to exploit superior tensile properties of Al/A206-5%Al_2O_3-Al_3Ti hybrid composites. In order to achieve this, intelligent techniques with superior process control such as high energy ball milling coupled with stir casting was employed. The effect of using this process for incorporation of reinforcing particles on final nano/microstructure and tensile properties of the composite, produced using a process involve milling and semi-solid stir casting, was explored.

2. Experimental procedure

Commercial aluminium (74 µm, supplied by Phoniex company), α-alumina (100 nm, supplied by Phoniex company) and K_2TiF_6 (60 µm, supplied by Aldrich company) powders were used in this study. Milling was performed in a Fritsch Pulverisette P5 planetary ball mill under argon gas (high purity, 99.999%) in a liquid

nitrogen environment (cryomilling). Rotation speed of the mill was kept about 480 rpm. In order to avoid excessive cold welding during milling, process control agent (PCA) was used (Stearic acid ($CH_3(CH_2)_{16}CO_2H$) powder was supplied by Merck).

To explore the behavior of K_2TiF_6 and aluminium powders against thermal exposure, differential scanning calorimetry (DSC) (at a rate of 10 $^{\circ}$C/min and under flowing argon) was utilized. Four powder samples were used; Aluminum powder, K_2TiF_6 powder, mixed mixture of aluminium and K_2TiF_6 powders and milled mixture of aluminium and K_2TiF_6 powders. Volumes of mixed and milled aluminium/K_2TiF_6 powder blends were heated in a tube furnace at a rate of 10 $^{\circ}$C/min (similar to DSC experiment) to temperatures corresponding to each major DSC signals for 1/2 h and subsequently quenched to room temperature to avoid microstructural changes during cooling.

X-ray diffraction (XRD) analysis was performed on heat treated powders to determine possible reaction corresponding to each DSC signal. XRD analysis was performed using PHILIPS-binary diffractometer applying Cu Ka radiation.

A206/5 % alumina$_p$-Al_3Ti hybrid composites were fabricated according to the following procedure: Initially, 99.7% pure aluminium, Cu and aluminium-80%Mn ingots were charged to the furnace and melted. After entire alloy in the crucible was melted, it was cooled down to 640°C. This temperature lies in the solid-liquid range and corresponds to solid fraction of about 0.2. Then, stirring of the semi-solid alloy was initiated in 400 rpm, while prepared powders were injected in to the uniformly formed vortex over a time period of approximately 5 min. Simultaneously, the non-contact ultrasonic casting method was utilized in order to apply vibration into the prepared melt. It consists of an ultrasonic chamber (Bandelin-Germany Make – Model: RK – 100H), which can vibrate at a frequency of 35 kHz. Powder injection into molten A206 aluminium alloy was performed under high purity argon atmosphere (99.999%, 6 lit/min). Two different architectures were utilized to incorporate reinforcing particle into semi solid alloy, i.e. (i) ball milling of K_2TiF_6 and aluminium powder for 5 h and subsequently with alumina for 1 h (denoted herein as $(K_2TiF_6+Al)_{(5h)}+Al_2O_{3(1h)}$) and (ii) ball milling of K_2TiF_6, aluminum and alumina powder for 2 h (denoted herein as $(K_2TiF_6+Al+Al_2O_3)_{(2h)}$). Indexes in parenthesis, hereafter, referred to milling time.

A proper mixture of the mentioned composition was selected so that after introducing powders in to the melt, melt composition reach to A206 alloy (Cu=4.20-5.00, Mg=0.20-0.35, Mn=0.20-0.50, Fe=0.07 max, Ni=0.03 max and Al=balance). After completion of particle injection, mixing was continued for extra 2 min. Finally, the composite slurry was poured into a pre-heated mould by using a bottom-pouring system. The composites fabricated via technique (i) denoted herein as A206-$(K_2TiF_6+Al)_{(5h)}+Al_2O_{3(1h)}$ and that of prepared via technique (ii) as A206-$(K_2TiF_6+Al+Al_2O_3)_{(2h)}$.

Morphology evolution of powders during milling and microstructure of the composite were studied by Field Emission Scanning Electron Microscopy (FE-SEM) performed in a HITACHI S4160, equipped with an energy dispersive X-ray analysis (EDX) accessory and Transmission Electron Microscopy ((TEM) Philips CM200).

Tensile testing was carried by a Hounsfield universal test machine at a cross-head speed of 0.5 mms^{-1}. The dog-bone shaped tensile specimens had a gauge size of 6 mm in diameter and 30 mm in length, according to ASTM: B557M-10.

3. Results and discussion

3.1. Thermal response of powders

Fig. 1a shows DSC pattern of K_2TiF_6 salt, evincing three endothermic signals. Signals 1, 2 and 3, as demonstrated in Fig. 1a, was appeared around 360 °C, 610 °C and 840 °C, respectively. Figs. 2 a and b exhibit XRD patterns of K_2TiF_6 salt held isothermally above signal 1 and 2 for 30 min at 450 °C and 650 °C, respectively, revealing K_2TiF_6 reflections alone. It is thus authenticated that K_2TiF_6 salt is stable up to 650 °C. The endothermic signals 1 and 2 are ascribed to the melting of impurities in K_2TiF_6 salt and that of signal 3 to the melting of K_2TiF_6 salt.

Fig. 1b shows DSC pattern of aluminum powder, evincing a single endothermic peak around 660 °C (signal 4) attributed to the melting of aluminum.

Fig. 1c shows DSC pattern of mixed mixture of aluminum and K_2TiF_6 salt. As is observed, by considering signal 5, DSC pattern of the mixture is not a simple superimposition of aluminum and K_2TiF_6. Signal 6 is ascribed to the melting of aluminum and K_2TiF_6 salt (between 630 °C and 650 °C).

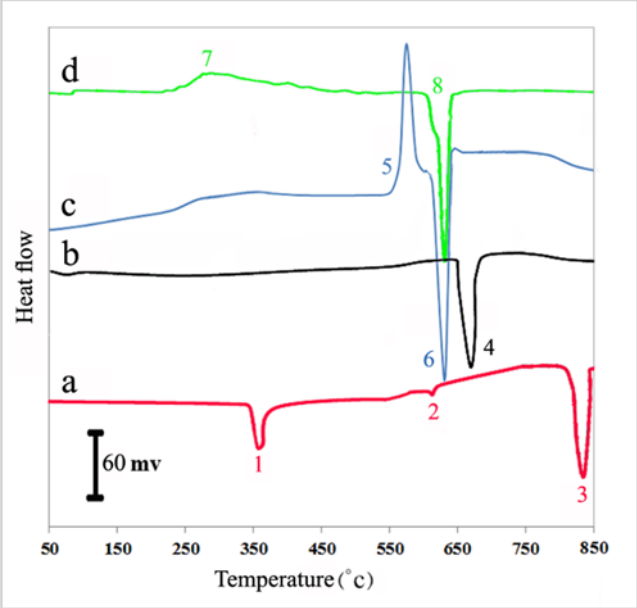

Fig. 1. DSC patterns of (a) K_2TiF_6 salt, (b) aluminum powder, (c) mixed mixture of aluminum and K_2TiF_6 salt and (d) milled mixture of aluminum and K_2TiF_6 salt.

Fig. 2c shows XRD pattern of mixed mixture of aluminum and K_2TiF_6 salt held isothermally below signal 5, evincing aluminum and K_2TiF_6 reflections. It can be concluded that aluminum and K_2TiF_6 has not reacted with each other up to this temperature.

Fig. 2d demonstrates XRD pattern of mixed mixture of aluminum and K_2TiF_6 salt held isothermally at 600 °C. It can be deduced that signal 5 is responsible for reaction 1:

$$3\ K_2TiF_6 + 13Al \rightarrow 3Al_3Ti + 3KAlF_4 + K_3AlF_6 \qquad (1)$$

FE-SEM image was also validated the formation of Al_3Ti in this temperature range (Fig. 3a). As is observed, Al_3Ti particles fused together in aluminum matrix.

Signal 6 in Fig. 1c is attributed to the melting of fluoride salts produced by reaction (1).

Fig. 1d shows DSC pattern of milled mixture of aluminium and K_2TiF_6 powder. The endothermic signal 7 starts at 220 °C and broaden to 450 °C. Signal 8 has also the same behavior as signal 6.

Fig. 2e shows XRD pattern of milled mixture of aluminium and K_2TiF_6 powder held isothermally above signal 7 (550 °C), evincing Al_3Ti, $KAlF_4$ and K_3AlF_6 in addition to those of aluminium. It is thus inferred that XRD pattern of milled mixture of aluminium and K_2TiF_6 powder held isothermally at 550 °C is the same as

that of mixed mixture of aluminium and K_2TiF_6 powder held isothermally at 600 ˚C. XRD spectrum of milled aluminium/K_2TiF_6 powders heat treated at 550 ˚C, after the completion of signal 7, is identical to that of the aluminium/ K_2TiF_6 mixture heat treated at 600 ◦C, with Al_3Ti, $KAlF_4$ and K_3AlF_6 reflections in addition to those of aluminium (Fig. 2e). Thus, it can be deduced that signal 7 is responsible for reaction (1). As such, signal 8 to the melting of $KAlF_4$ and K_3AlF_6, produced by reaction (1). The formation of Al_3Ti is also validated in the milled mixture of aluminium/K_2TiF_6 powders heat treated at 350 ˚C (Fig. 3b). Comparing Figs. 3a with 3b reveal the difference between morphology of Al_3Ti particles. Al_3Ti particles in the former are relatively coarser than in the latter.

This change in the morphology of Al_3Ti particles and the shift of reaction (1) to 220 ˚C-450 ˚C in the milled mixture, authenticates that the milling process facilitates K_2TiF_6/aluminium interaction.

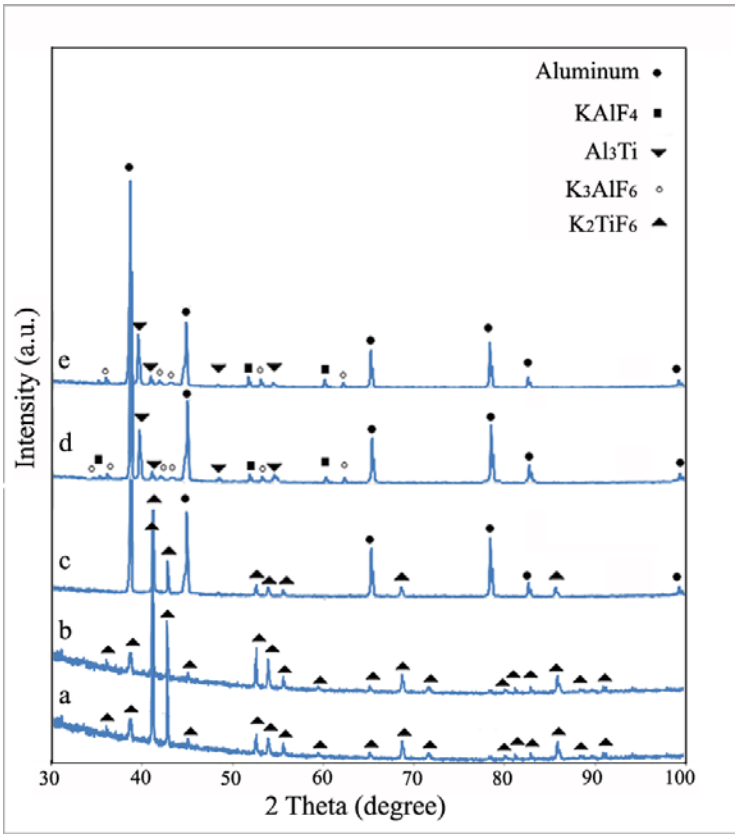

Fig. 2. XRD patterns of (a) K_2TiF_6 salt held isothermally above signal 1 in Fig. 1, (b) K_2TiF_6 salt held isothermally above signal 2 in Fig.1, (c) mixed mixture of aluminium/K_2TiF_6 heat treated below signal 5 in Fig.1, (d) mixed mixture of aluminium/K_2TiF_6 heat treated above signal 5 in Fig.1 and (e) milled mixture of aluminium/K_2TiF_6 powders heat treated above signal 7 in Fig. 1.

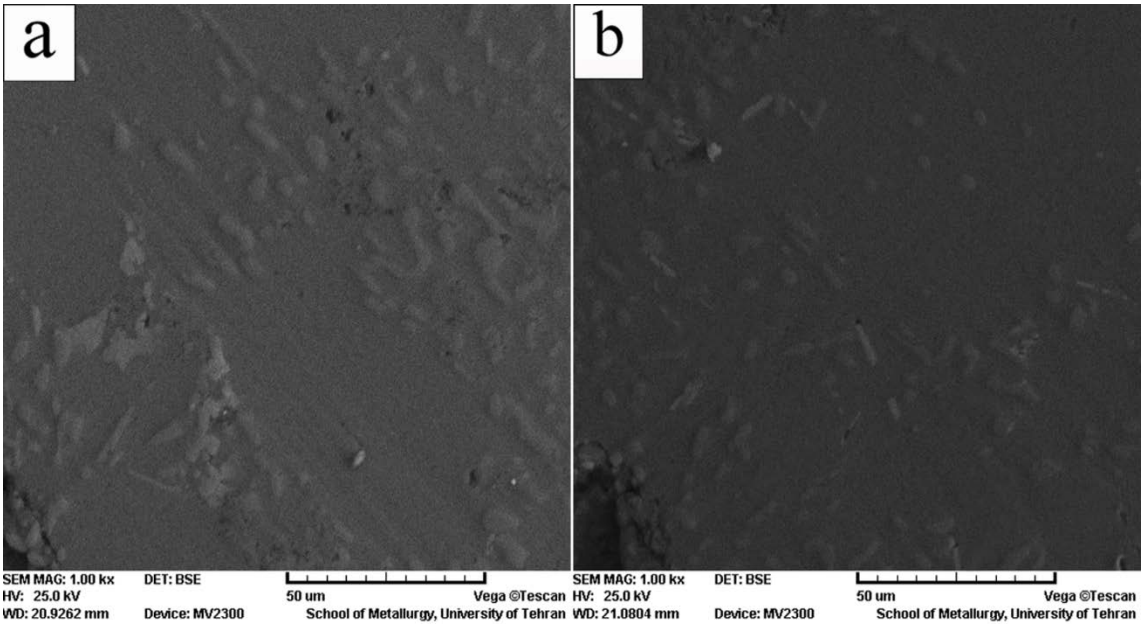

Fig. 3. Morphology of (a) mixed mixture of aluminum and K_2TiF_6 salt held isothermally at 600 ˚C and (b) milled mixture of aluminum and K_2TiF_6 salt held isothermally at 350˚C.

It is therefore plausible to use this unique process for synthesizing in situ/ex situ MMCs using melt processing routes. By considering the fact that milling alleviates the formation temperature of Al_3Ti particles, inferior casting temperature can be utilized. Furthermore, as mentioned above, interaction between K_2TiF_6 and aluminium facilitates. In addition, this unique process has another surprising capacity in changing the morphology and distribution of Al_3Ti particles.

3.2. Morphology of milled powders

Fig. 4 shows the morphology of K_2TiF_6 (Fig. 4a), $(K_2TiF_6+Al+Al_2O_3)_{(2h)}$ (Figs. 4b and c), $(K_2TiF_6+Al)_{(2h)}$ (Fig. 4d) and $(K_2TiF_6+Al)_{(5h)}+Al_2O_{3\,(1h)}$ (Fig. 4e), respectively.

Figs. 5a and b show XRD pattern of milled powders corresponding to Figs. 4b and e, respectively. Results of XRD analysis relieved $KAlF_4$, K_3AlF_6 and Al_3Ti in the case of $(K_2TiF_6+Al)_{(5h)}+Al_2O_{3(1h)}$ and K_2TiF_6, aluminium and Al_2O_3 in the case of $(K_2TiF_6+Al+Al_2O_3)_{(2h)}$. SAD patterns in Figs. 4b and e also confirmed the above findings.

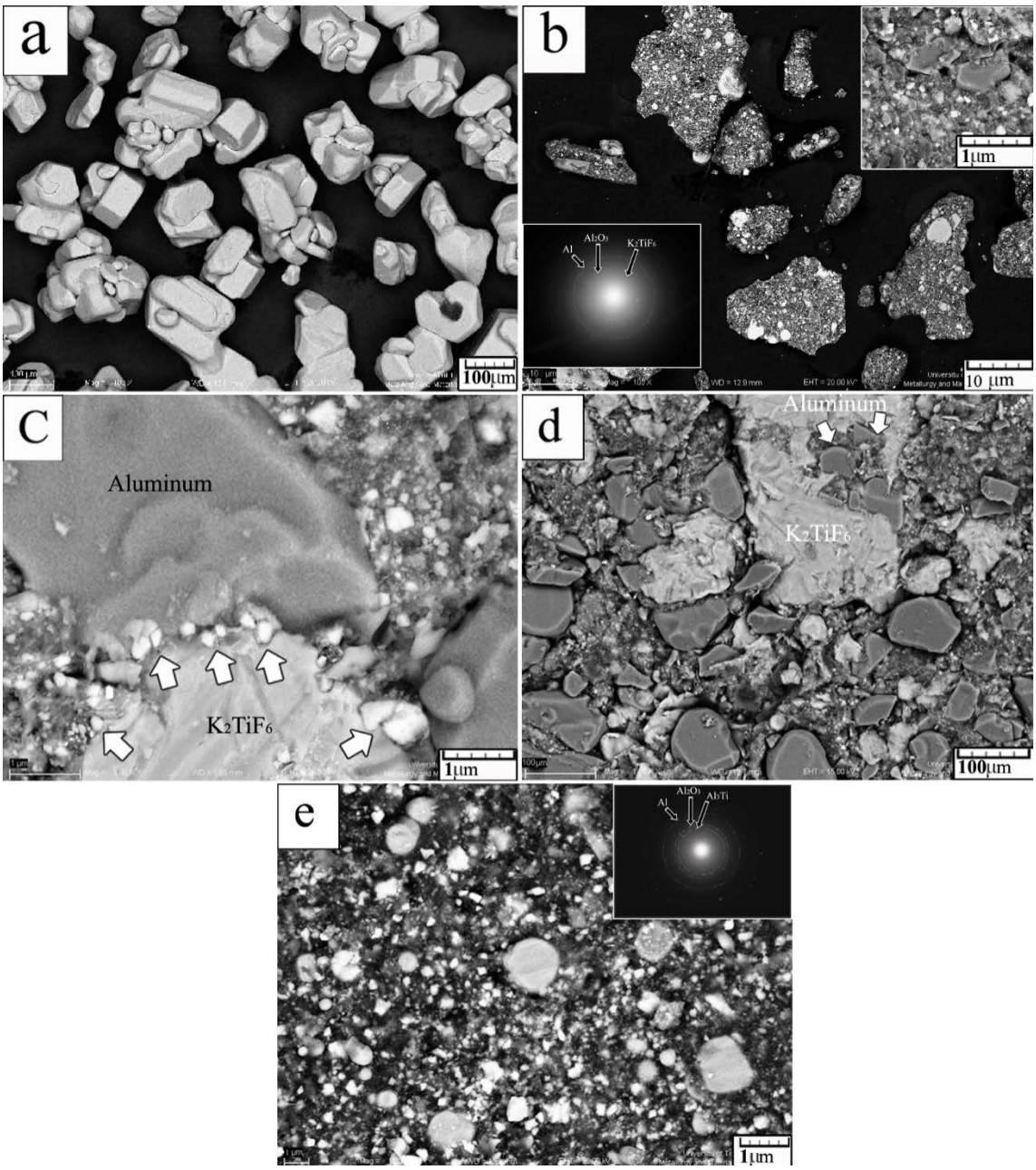

Fig. 4. Morphology of (a) K_2TiF_6, (b) $(K_2TiF_6+Al+Al_2O_3)_{(2h)}$, (c) higher magnification of b, (d) $(K_2TiF_6+Al)_{(2h)}$, (e) $(K_2TiF_6+Al)_{(5h)}+Al_2O_3$ $_{(1h)}$.

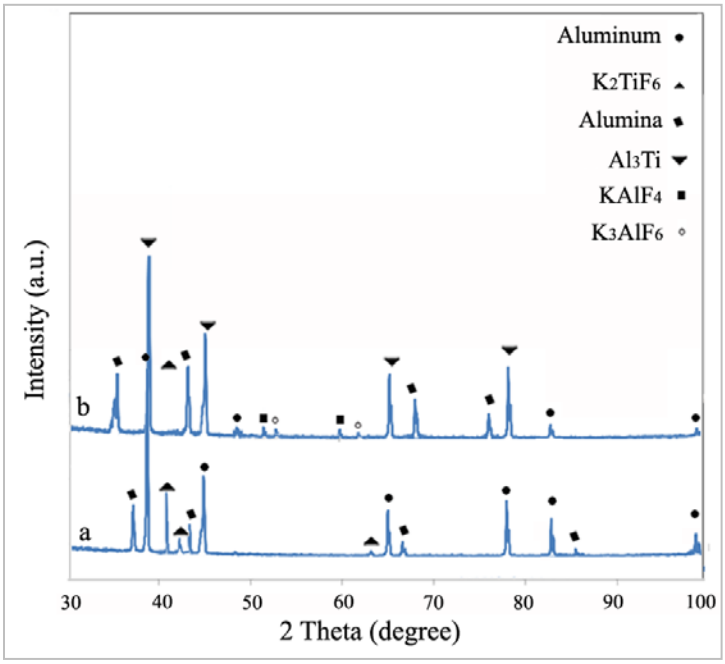

Fig. 5. XRD patterns of (a) $(K_2TiF_6+Al+Al_2O_3)_{(2h)}$, (b) $(K_2TiF_6+Al)_{(5h)}+Al_2O_{3\,(1h)}$.

In the case of $(K_2TiF_6+Al+Al_2O_3)_{(2h)}$ powder, nano alumina particles adhered to the sharp corners of K_2TiF_6 powder (white arrows on Fig. 4c) which inhibiting the intimate contact between aluminium and K_2TiF_6 powders and therefore impeding Al_3Ti formation. Thus, in order to prepare a suitable condition for the formation of Al_3Ti, at first, K_2TiF_6 and aluminium powders were milled and then alumina powder were added to the ball mill vial. As is observed in Fig. 4d, K_2TiF_6 and aluminium powders are in close contact with each other after 2 h milling time. After 5 h milling and addition of aluminium powder and milling for 1 h (Fig. 4e), the mixture contains Al_3Ti, $KAlF_6$, K_3AlF_6 and alumina (Fig. 5b).

On the other hand, in the case of $(K_2TiF_6+Al+Al_2O_3)_{(2h)}$, as is observed in Fig. 4b, milled powders are integrated into capsule-shaped particles. During semi solid stir casting, capsule-shaped particles are disintegrated into molten alloy. The size of capsule-shaped particles after milling is lower than 20 µm that can accommodate better dissolution and lower agglomeration of them during subsequent semi-solid stir casting. Furthermore, inset in Fig. 4b, evincing cross section of capsule-shaped particles, substantiating uniform distribution of alumina particles inside them. In the other words, alumina particle were distributed not only on the outer surface of capsule-shaped particles but well-distributed underneath the surface.

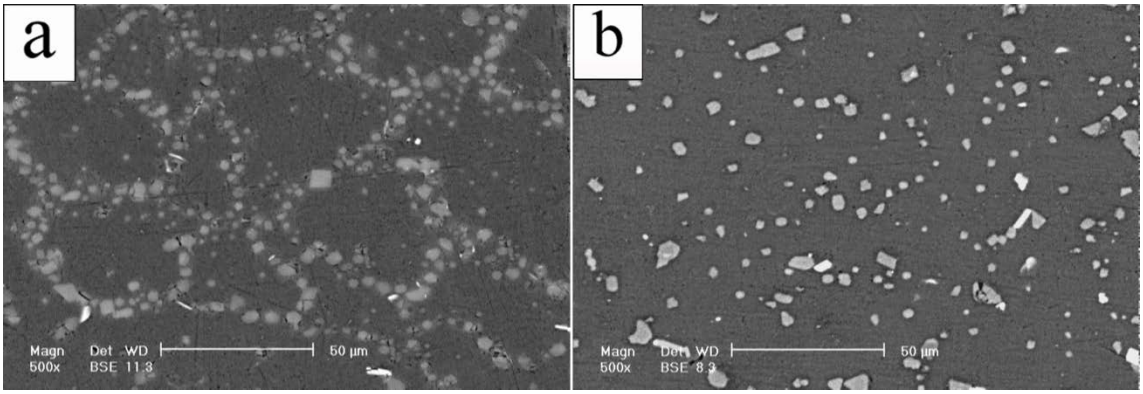

Fig. 6. Morphology of alumina and Al_3Ti particles in (a) A206-$(K_2TiF_6+Al)_{(5h)}+Al_2O_{3(1h)}$ and (b) A206-$(K_2TiF_6+Al+Al_2O_3)_{(2h)}$ composites.

3.3. Composite microstructure

Figs. 6a and b show FE-SEM microstructures of A206-$(K_2TiF_6+Al)_{(5h)}+Al_2O_{3(1h)}$ and A206-$(K_2TiF_6+Al+Al_2O_3)_{(2h)}$ composites, respectively. As is observed, the size of Al_3Ti as well as the distribution of Al_3Ti and alumina particulates is not the same. Figs. 7a, b and c show HRTEM images of A206-$(K_2TiF_6+Al)_{(5h)}+Al_2O_{3(1h)}$, high magnification of (a) and schematic illustration of (a), respectively. Figs. 7d, e and f show HRTEM images of A206-$(K_2TiF_6+Al+Al_2O_3)_{(2h)}$ composites, high magnification of (d) and schematic illustration of (d), respectively. As can be seen in Figs.7a and c, the majority of alumina and Al_3Ti particles in A206-$(K_2TiF_6+Al)_{(5h)}+Al_2O_{3(1h)}$ sample have a high propensity to reside in grain boundaries instead of grain interior. However, according to Figs. 7d and f, in the case of A206-$(K_2TiF_6+Al+Al_2O_3)_{(2h)}$ sample, the majority of well-dispersed alumina and Al_3Ti particles are resided in the grain interior rather than grain boundaries, ascribed to following effects.

By introducing $(K_2TiF_6+Al+Al_2O_3)_{(2h)}$ powders into molten alloy, three interesting phenomenon will occur: Firstly, aluminum powder in capsule-shaped particles melts and releases K_2TiF_6 and alumina particles into the melt. K_2TiF_6 reacts with metal melt by exothermic reaction 1, leading to local increment in temperature. This local increase in temperature fortifies the wettabilty of nano alumina particle with molten alloy as well as the willingness to particle engulfment [28].

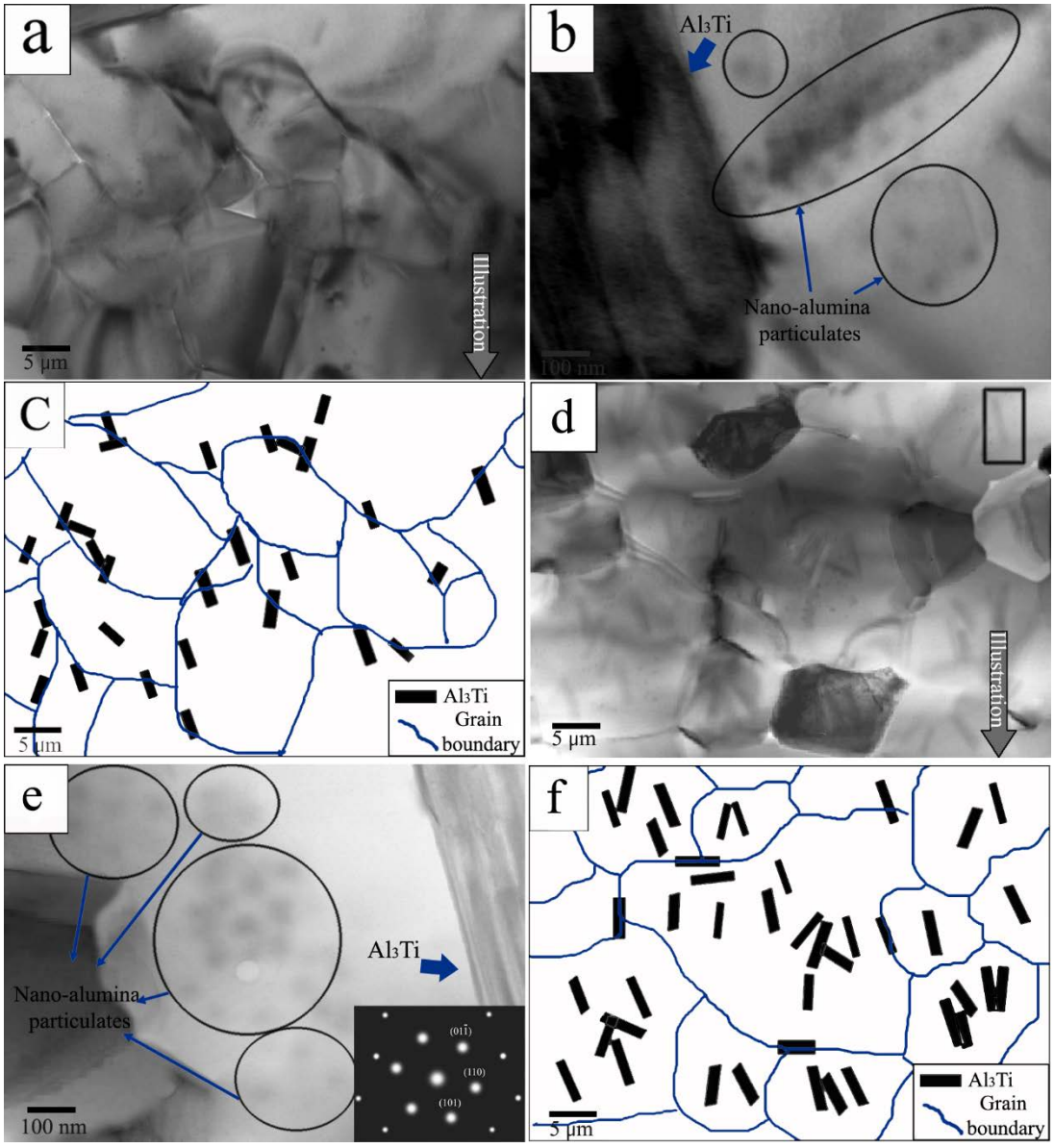

Fig. 7. (a) HRTEM images of A206-$(K_2TiF_6+Al)_{(2h)}+Al_2O_{3(1h)}$, (b) higher magnification of (a), (c) schematics illustration of (a), (d) HRTEM images of A206-$(K_2TiF_6+Al+Al_2O_3)_{(5h)}$ composites, (e) higher magnification of specified region in (d) and (f) schematics illustration of (d).

Secondly, as result of reaction between K_2TiF_6 and molten alloy, fluorides components (according to reaction 1) release to the melt leading to removing oxide layer on the melt surface [29], which enhances the wettabilty of nano alumina particle with molten alloy [30-32].

Secondly, Al_3Ti has tetragonal structure with lattice parameters of a=0.3848 nm and c=0.8596 nm and α-Al has lattice parameter of a=0.4094 nm. Strain at interface in a and c direction is calculated through equation 2 and 3 [33]:

$$\varepsilon_{aa}=(1-a_{Al3Ti}/a_{Al})\times100=+4.96\% \quad (2)$$

$$\varepsilon_{cc}=(1-c_{Al3Ti}/2a_{Al})\times100=-6.15\% \quad (3)$$

These calculations authenticate that strain at interface is negligible and α-Al/Al_3Ti interface is coherent. In the other word, Al_3Ti is an appropriate site for secondary α-Al nucleation. Al_3Ti has (001) plane with the lowest strain mismatch with α-Al (012) plane. Therefore, it can be concluded that Al_3Ti is a suitable site for α-Al nucleation. Consequently, in the case of A206-$(K_2TiF_6+Al+Al_2O_3)_{(5h)}$, nucleation of Al_3Ti in molten alloy occurs simultaneously throughout the molten alloy results in the uniform distribution of Al_3Ti in the matrix. On the other hand, in the case of A206-$(K_2TiF_6+Al)_{(2h)}+Al_2O_{3(1h)}$ sample, when $(K_2TiF_6+Al)_{(2h)}+Al_2O_{3(1h)}$ is incorporated into semi solid alloy, Al_3Ti particles releases into molten alloy. As Al_3Ti particles have higher driving-power relative to alumina particles, they cut α-aluminum more easily (Fig. 8a), brings about residing Al_3Ti particles in grain boundaries (Fig. 7a and c). The resultant microstructure of A206-$(K_2TiF_6+Al)_{(2h)}+Al_2O_{3(1h)}$ composite is schematically shown in Fig. 8b. This composite demonstrates a microstructure with a unique combination of lean matrix region and reinforcement rich zone appeared in a network fashion around AlA206 matrix grain boundaries.

In the case of A206-$(K_2TiF_6+Al+Al_2O_3)_{(5h)}$ sample, when $(K_2TiF_6+Al+Al_2O_3)_{(5h)}$ is incorporated into semi solid alloy, aluminum powder in capsule-shaped particles melts and releases alumina particles into molten alloy. As stirring proceeds, alumina particles entraps by α-aluminum. This can be ascribed to the lower driving-power of fine alumina particles rather than that of agglomerated particles. As depicted schematically in Fig. 9a, agglomerated alumina particles have higher driving-power giving rise to cut through α-aluminum more easily. The driving-power of alumina particles may not be adequate to do the same, and they may become entrapped in α-aluminum grain interior, Fig. 9b. Resultantly, a microstructure mainly containing Al_3Ti and alumina in grains are formed, Fig. 9c. It is plausible to say that this hypothesis has a bottle neck in the case of A206-$(K_2TiF_6+Al)_{(2h)}+Al_2O_{3(1h)}$ where local increment in temperature is not co-exist to fortify driving-power of alumina particles in such a manner that observed in A206-$(K_2TiF_6+Al+Al_2O_3)_{(5h)}$ sample.

Resultantly, in A206-$(K_2TiF_6+Al)_{(2h)}+Al_2O_{3(1h)}$ sample, alumina particles were mainly found in grain boundaries. Therefore, this microstructure possesses a unique combination of alumina and Al_3Ti in grain boundaries.

Another difference between A206-$(K_2TiF_6+Al+Al_2O_3)_{(5h)}$ and A206-$(K_2TiF_6+Al)_{(2h)}+Al_2O_{3(1h)}$ is related to the size of Al_3Ti particles. Al_3Ti is smaller in the latter. Because in the former, Al_3Ti is formed in situ in the semi solid state while in latter Al_3Ti has been formed before powder addition (in the milling process). Temperature in the semi solid state is more enough to enlarge the in situ formed Al_3Ti particles. However, in the case of A206-$(K_2TiF_6+Al)_{(2h)}+Al_2O_{3(1h)}$, Al_3Ti particles was formed in the milling process. Ball mill has high enough energy to break Al_3Ti particles.

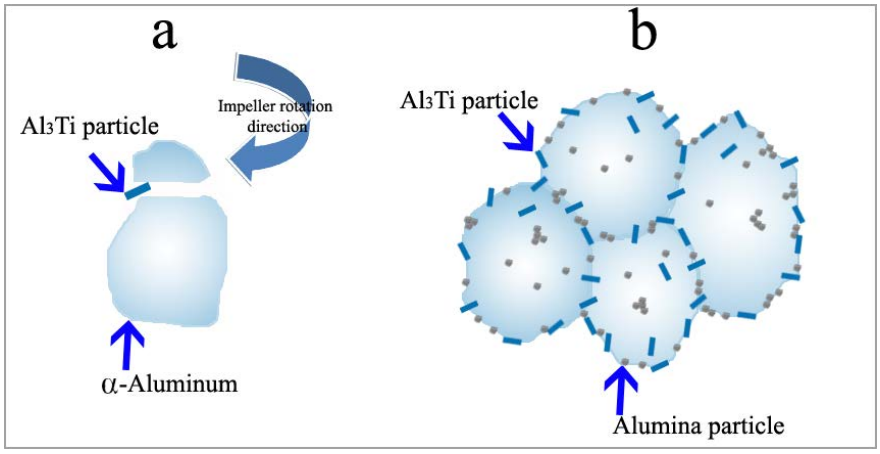

Fig. 8. Schematic illustration showing the distribution of (a) Al_3Ti particle and (b) final microstructure of A206-$(K_2TiF_6+Al)_{(2h)}+Al_2O_{3(1h)}$.

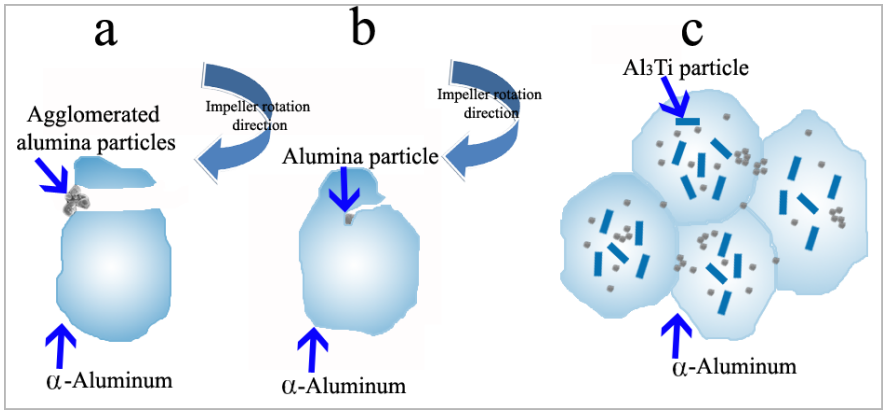

Fig. 9. Schematic illustration showing the distribution of (a) agglomerated alumina particle, (b) alumina particle and (c) final microstructure of A206-$(K_2TiF_6+Al+Al_2O_3)_{(5h)}$.

It is worth nothing that in the case of A206-$(K_2TiF_6+Al+Al_2O_3)_{(5h)}$ sample, a composite containing ex situ alumina particle and in situ Al_3Ti particles was successfully tailored while in the case of A206-$(K_2TiF_6+Al)_{(5h)}+Al_2O_{3(1h)}$, a composite containing ex situ alumina and Al_3Ti particles was formed.

3.4. Tensile properties

Fig. 10 shows tensile properties of A206, A206-$(K_2TiF_6+Al+Al_2O_3)_{(5h)}$ and A206-$(K_2TiF_6+Al)_{(2h)}+Al_2O_{3(1h)}$ samples. As is observed, $Al_2O_{3np}+Al_3Ti_p$ improved tensile properties of AlA206 alloy, significantly.
On the other hand, it can be observed that A206-$(K_2TiF_6+Al)_{(2h)}+Al_2O_{3(1h)}$ network-structure composite containing Al_3Ti_P and Al_2O_{3np} displays superior strength compared to A206-$(K_2TiF_6+Al+Al_2O_3)_{(5h)}$ composite. A206-$(K_2TiF_6+Al)_{(2h)}+Al_2O_{3(1h)}$ composite shows 80.1% and 20.69% increase in ultimate tensile strength when compared to the as-received A206 and A206-$(K_2TiF_6+Al+Al_2O_3)_{(5h)}$ composite, respectively. These augmented tensile properties can be ascribed to the unique microstructure of the composite which contains two phases, as shown in Fig. 7a. The enhanced tensile properties of A206-$(K_2TiF_6+Al)_{(5h)}+Al_2O_{3(1h)}$ network-structure composite can be explicated by the (H-S) theorem (Hashin-Shtrikman) [34] where $Al_3Ti_P+Al_2O_{3np}$ stronger phase surrounds AlA206 matrix weaker phase. On the other word, Al_3Ti_P and Al_2O_{3np} concentrated around grain boundaries of AlA206 matrix, act as a composite with high volume fraction of $Al_3Ti_P+Al_2O_{3np}$. Resultantly, the surprising feature of this unique structure is a matrix with fortified grain boundaries. In such a structure, dispersed high local $Al_3Ti_P+Al_2O_{3np}$ in grain boundaries produces a synergistic effect via forming a three-dimension skeletal structure. The resistance to slip in such structure is high because this unique structure has a main contribution in barricading dislocation movement. That is to say, A206-$(K_2TiF_6+Al)_{(5h)}+Al_2O_{3(1h)}$ network-structure composite containing reinforcing particles around grain boundaries can effectively strengthen grain boundaries by enhancing dislocation accumulation density during tensile deformation (Figs. 11 a and b).

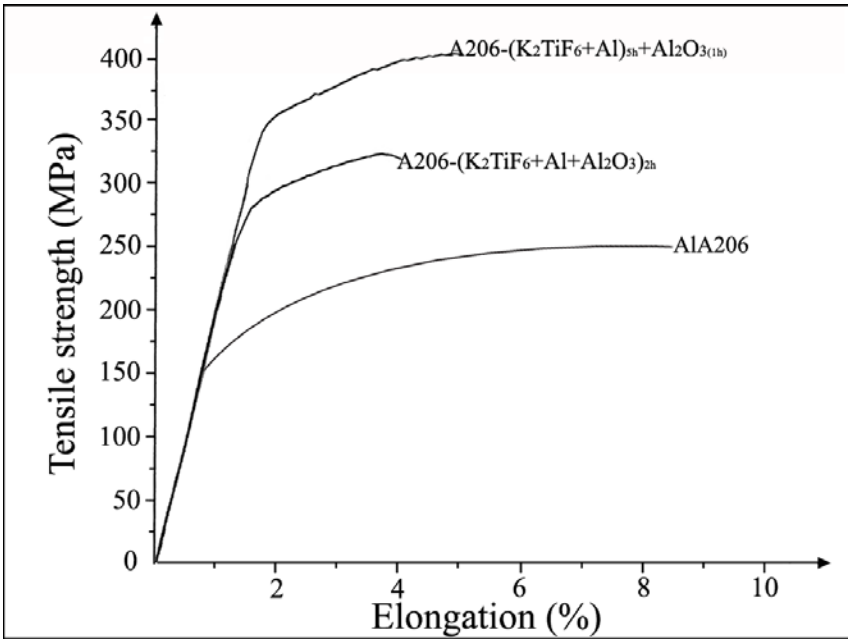

Fig. 10. Tensile properties of AlA206, A206-$(K_2TiF_6+Al+Al_2O_3)_{(5h)}$ and A206-$(K_2TiF_6+Al)_{(2h)}+Al_2O_{3(1h)}$ composites.

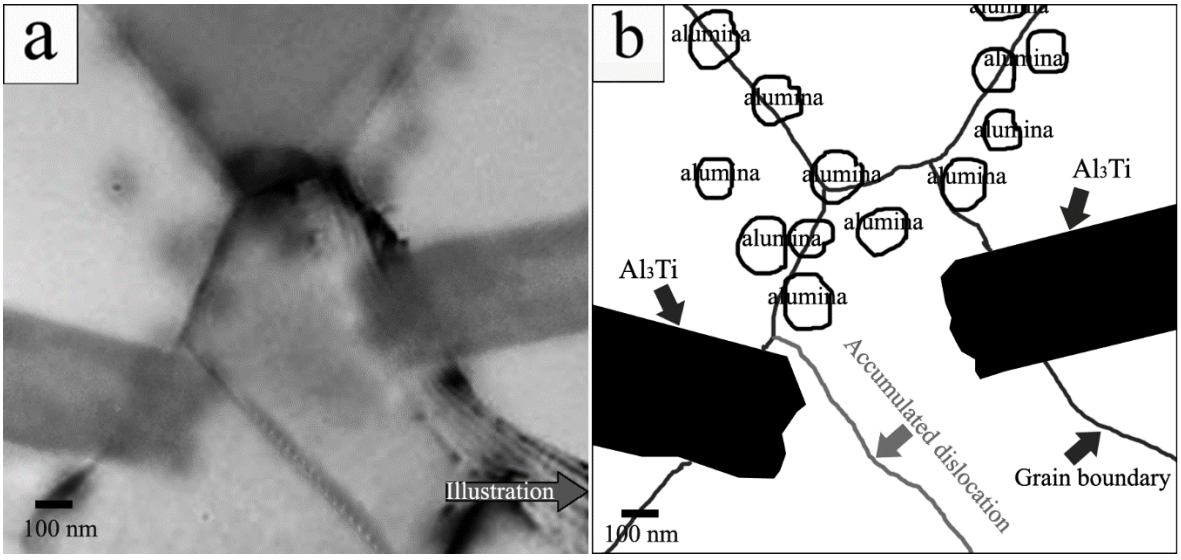

Fig. 11. (a) HRTEM images of A206-$(K_2TiF_6+Al)_{(2h)}+Al_2O_{3(1h)}$ composite exhibiting dislocation accumulation behind grain boundary and (b) schematic illustration of (a).

3.4.1. Fracture behavior

Fig. 12 shows fracture side views of a network-structure A206-$(K_2TiF_6+Al)_{(5h)}+Al_2O_{3(1h)}$ hybrid composite. Crack propagation occurs through $Al_3Ti_P+Al_2O_{3np}$ network-structure. Formation of micro-crack away from

fracture surface in reinforcement network-structure brings to mind two interesting phenomenon; firstly, crack propagation take place via micro-crack coalescence through reinforcement network-structure and secondly, crack propagation to matrix-lean region is effectively barricaded by Al_3Ti_P +Al_2O_{3np} network-structure (indicated by arrow), contributing to enhanced tensile strength of A206-$(K_2TiF_6+Al)_{(5h)}$+$Al_2O_{3(1h)}$ hybrid composite.

Fig. 13 shows fracture surface of a network-structure A206-$(K_2TiF_6+Al)_{(5h)}$+$Al_2O_{3(1h)}$ hybrid composite. As can be observed in Fig. 13a, there is no sign of large AlA206 matrix rupture, fortifying crack propagation through reinforcement network-structure.

As demonstrated in Fig. 13b, Al_3Ti particle showed brittle cleavage fracture confirming strong interfacial bonding strength between matrix and reinforcement and consequently load bearing capacity of the composite. In tensile test, as load is proceeding, dislocation pile-up at matrix/reinforcement results in initiation and fracture of these particles. Thus, matrix cracking extended in to Al_3Ti particle (indicated by arrow on Fig. 13b). Subsequently, AlA206 matrix experienced plastic deformation appeared in the form of dimples. Formation of such dimples further authenticating that AlA206 matrix is continuous and interpenetrating.

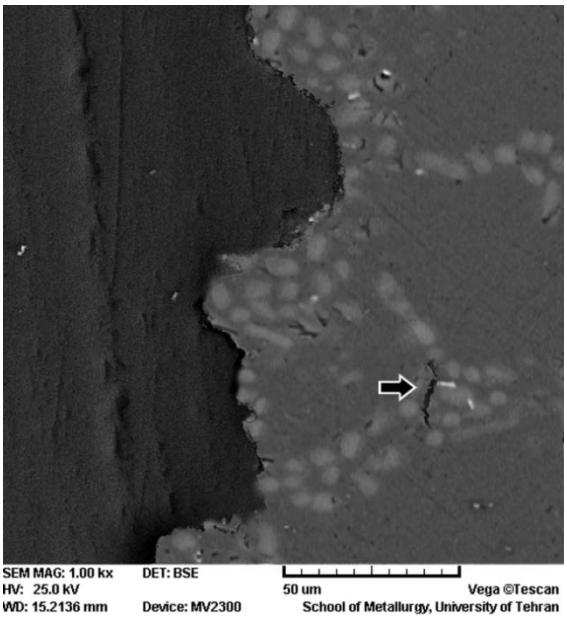

Fig. 12. Fracture side views of a network-structure A206-$(K_2TiF_6+Al)_{(5h)}$+$Al_2O_{3(1h)}$ hybrid composite.

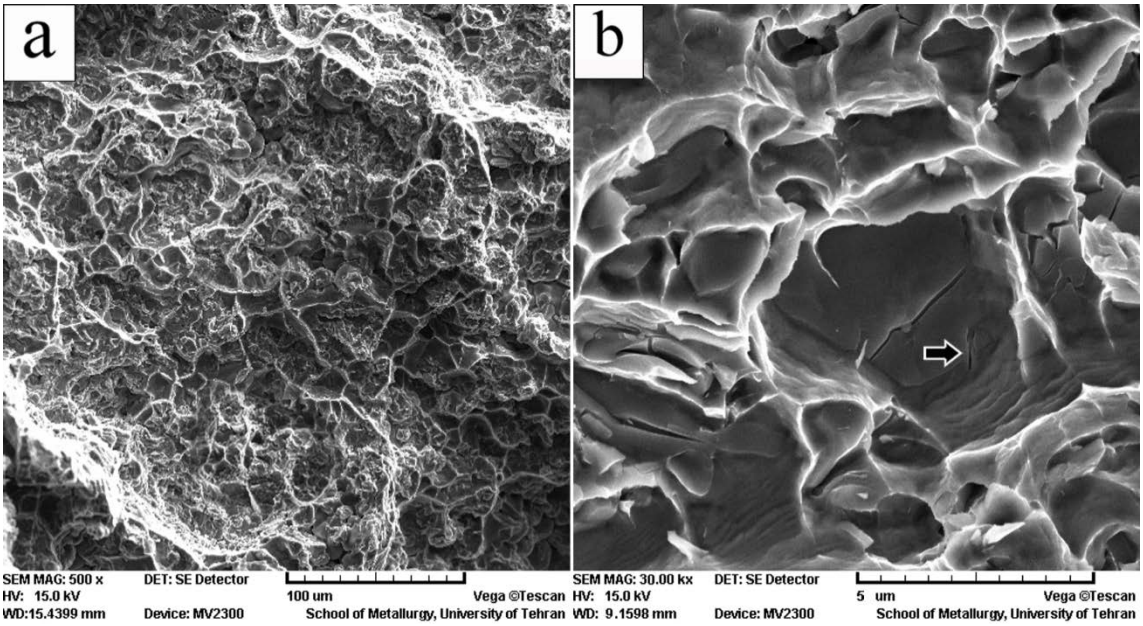

Fig. 13. Fracture behavior of a network-structure A206-$(K_2TiF_6+Al)_{(5h)}+Al_2O_{3(1h)}$ hybrid composite, (a) overall view and (b) Al_3Ti particle cracking.

4. Conclusions

Al/A206-5%Al_2O_3-Al_3Ti hybrid composites were successfully synthesized using milled mixture of K_2TiF_6, alumina and aluminium powders and stir-casting technology. The following conclusions can be deduced:

1- Milling of $(K_2TiF_6+Al+Al_2O_3)_{(2h)}$ mixture impedes Al_3Ti formation, while milled mixture of $(K_2TiF_6+Al)_{(5h)}+Al_2O_{3(1h)}$ causes the formation of Al_3Ti particles.

2- Milling process reduced the formation temperature of Al_3Ti particles and changed the morphology of Al_3Ti particles.

3- Injection of Milled $(K_2TiF_6+Al+Al_2O_3)_{(2h)}$ mixture in semi solid alloy results in the formation of well-distributed alumina and Al_3Ti in grain interiors while $(K_2TiF_6+Al)_{(5h)}+Al_2O_{3(1h)}$ milled mixture, brings about the formation of a reinforcement network structure.

4- Formation of Al_3Ti with coherent interface in injected milled $(K_2TiF_6+Al+Al_2O_3)_{(5h)}$ mixture caused the uniform distribution of Al_3Ti in grain interior. Alumina nano particulate with low-driving power entrapped by α-aluminum and resided in grain interior.

5- In injected milled $(K_2TiF_6+Al)_{(5h)}+Al_2O_{3(1h)}$ mixture, released Al_3Ti in molten alloy had higher driving-power to cut α-aluminum and therefore, Al_3Ti resided in grain boundaries.

6- Network structured A206-$(K_2TiF_6+Al)_{(2h)}+Al_2O_{3(1h)}$ composite with fortified grain boundaries displayed superior tensile properties compared with $(K_2TiF_6+Al+Al_2O_3)_{(5h)}$ composite ascribed to fortified grain boundaries by $Al_3Ti_P+Al_2O_{3np}$.

References:

[1] Hoseini M, Meratian M. Fabrication of in situ aluminum-alumina composite with glass powder. J Alloy Compd 2009;471:378-382.

[2] Yilmaz O, Buytoz S. Abrasive wear of Al/Al_2O_3-reinforced aluminum-based MMCs. Compos Sci Technol 2001;61:2381-2392.

[3] Al-Qutub AM, Allam IM, Qureshi TW. Effect of sub-micron Al_2O_3 concentration on dry wear properties of 6061 aluminum based composite. J Mater Process Tech 2006;172:327-331.

[4] Ye J, He J, Schoenung JM. Cryomilling for the fabrication of a particulate B_4C reinforced Al nanocomposite: Part I. Effects of process conditions on structure. Metall Mater Trans A 2006;37A:3099-3109.

[5] Kawabata K, Sato E, Kuribayashi K. Creep deformation behavior of spherical Al_2O_3 particle reinforced Al–Mg matrix composites at high temperatures. Acta Mater 2002;50:3465-3474.

[6] Yao-Hui L, Jun D, Si-Rong Y, Wei W. High temperature friction and wear behavior of Al_2O_3 and/or carbon short fibre reinforced Al–12Si alloy composites. Wear 2004;256:275-285.

[7] Del-Rio E, Nash JM, Williams JC, Breslin MC, Daehn GS. Co-continuous composites for high temperature applications. Mater Sci Eng A 2007;463:115-121.

[8] Mahdavi S, Akhlaghi F. Effect of SiC content on the processing, compaction behavior, and properties of Al6061/SiC/Gr hybrid composites. J Mater Sci 2011;461:1502-1511.

[9] Tjong SC, Mai YW. Processing-structure-property aspects of particulate- and whisker-reinforced titanium matrix composite. Compos Sci Technol 2008;68:583-601.

[10] Qin S, Zhang G. Preparation of high fracture performance SiC_p-6061A1/6061A1 composite. Mater Sci Eng A 2000;279:231-236.

[11] Segurado J, Gonzalez C, Llorca J. A numerical investigation of the effect of particle clustering on the mechanical properties of composites. Acta Mater 2003;51:2355-2369.

[12] Wilkinson DS, Pompe W, Oeschner M. Modeling the mechanical behaviour of heterogeneous multi-phase materials. Prog Mater Sci 2001;46:379-405.

[13] Peng HX, Fan Z, Evans JRG. Bi-continuous metal matrix composite. Mater Sci Eng A 2001;303:37-45.

[14] Scherm F, Völkl R, Van Smaalen S, Mondal S, Plamondon P, L'Espérance G, Bechmann F, Glatzel U. Microstructural characterization of interpenetrating light weight metal matrix composites. Mater Sci Eng A 2009;518:118-123.

[15] Huang LJ, Geng L, Peng HX, Zhang J. Room temperature tensile fracture characteristics of in situ TiBw/Ti_6Al_4V composites with a quasi-continuous network architecture. Scr Mater 2011;64:844-847.

[16] Huang LJ, Geng L, Peng HX, Kaveendran B. High temperature tensile properties of in situ TiBw/Ti_6Al_4V composites with a novel network reinforcement architecture. Mater Sci Eng A 2012;534:688-692.

[17] Huang LJ, Geng L, Wang B, Xu HY, Kaveendran B. Kaveendran. Effects of extrusion and heat treatment on the microstructure and tensile properties of in situ TiB_w/Ti_6Al_4V composite with a network architecture. Compos PartA Appl Sci Manuf 2012;43:486-491.

[18] Huang LJ, Wang S, Dong YS, Zhang YZ, Pan F, Geng L, Peng HX. Tailoring a novel network reinforcement architecture exploiting superior tensile properties of in situ TiB_w/Ti composites. Mater Sci Eng A 2012;545:187-193.

[19] Huang LJ, Wang S, Geng L, Kaveendran B, Peng HX. Low volume fraction in situ (Ti_5Si_3 + Ti_2C)/Ti hybrid composites with network microstructure fabricated by reaction hot pressing of Ti–SiC system. Compos Sci Technol 2013;82:23-28.

[20] Tjong SC, Ma ZY. Microstructural and mechanical characteristics of in situ metal matrix composites. Mater Sci Eng R 2000;29:49-113.

[21] Zhao YT, Zhang SL, Chen G, Cheng XN, Wang CQ. In situ $(Al_2O_3 + Al_3Zr)_{np}$/Al nanocomposites synthesized by magneto-chemical melt reaction. Compos Sci Technol 2008;68:1463-1470.

[22] Zhu H, Min J, Li J, Ai Y, Ge L, Wang H. In situ fabrication of (α-$Al_2O_3 + Al_3Zr$)/Al composites in an Al–ZrO_2 system. Compos Sci Technol 2010;70:2183-2189.

[23] El-Hadad S, Sato H, Watanabe Y. Wear of Al/Al_3Zr functionally graded materials fabricated by centrifugal solid-particle method. J Mater Process Technol 2010;210:2245-2251.

[24] Ferreira SC, Rocha LA, Ariza E, Sequeira PD, Watanabe Y, Fernandes JCS. Corrosion behaviour of Al/Al_3Ti and Al/Al_3Zr functionally graded materials produced by centrifugal solid-particle method: Influence of the intermetallics volume fraction. Corros Sci 2011;53:2058-2065.

[25] Varin RA. Intermetallic-reinforced light-metal matrix in-situ composites. Metall Mater Trans A 2002;33A:193-201.

[26] Ward-Close CM, Minor R, Doorbar PJ. Intermetallic-matrix composites-a review. Intermetallics 1996;4:217-229.

[27] Mahendra KV, Radha Krishna K. Characterization of Stir Cast Al Cu (fly ash + SiC) hybrid metal matrix composites. J Com Mate 2010;44(8):989-1005.

[28] Tahamtan S, Halvaee A, Emamy M, Zabihi MS. Fabrication of Al/A206–Al_2O_3 nano/micro composite by combining ball milling and stir casting technology. Mater Design 2013;49:347-359.

[29] Kalaiselvan K, Murugan N, Parameswaran S. Production and characterization of AA6061–B_4C stir cast composite. Mater Design 2011;32:4004-4009.

[30] Toptan F, Kilicarslan A, Cigdem M, Kerti I. Processing and microstructural characterization of AA1070 and AA 6063 matrix B_4C_p reinforced composites. Mater Des 2010;31:87-91.

[31] Kerti I, Toptan F. Microstructural variations in cast B_4C-reinforced aluminium matrix composites (AMCs). Mater Lett 2008;62:1215-1228.

[32] Kennedy AR, Brampton B. The reactive wetting and incorporation of B_4C particles into molten aluminium. Scripta Mater 2001;44:1077-1082.

[33] Sankaranarayanan S, Jayalakshmi S, Gupta M. Effect of ball milling the hybrid reinforcements on the microstructure and mechanical properties of Mg-(Ti+n-Al_2O_3) composites. J Alloy Compd 2011;509:7229-7237.

[34] Clyne TW, Withers PJ. An Introduction to Metal Matrix Composites. Cambridge University Press: UK, Cambridge; 1993.